Chapter 4

VCSELs with monolithically integrated metasurfaces

This chapter details the characteristics of the fabricated bottom-emitting MS-VCSELs. In **Fig. 4.1**, an SEM image of the metasurface side of an MS-VCSEL chip with 81 different metasurfaces can be seen. On the other side of the chip, each metasurface has a corresponding individually addressable VCSEL that can illuminate the metasurfaces. While this monolithic approach yields a compact, integrable, and mechanically robust light source, it fixes the propagation distance between the VCSEL cavity and the metasurface. Therefore, the beam waist of the light incident on the metasurface is predetermined, which in turn limits the NA for any integrated optics. Furthermore, etching without a dedicated etch-stop layer means all metasurface fabrication is subject to ARDE, which significantly limits metasurface design, particularly for dynamic-phase metasurfaces. In addition, careful handling and protection of the VCSEL substrate side is crucial since the metasurface will be integrated on this delicate surface.

4.1 Dynamic-phase MS-VCSELs

As mentioned in the previous chapter, ARDE has constrained the fabrication of monolithically integrated dynamic-phase metasurfaces. Without an etch stop, ARDE induces depth variations depending on the gaps between different metaatoms. This impairs the approximated phase profile and yields different optical artifacts when etching dynamic-phase metasurfaces into the VCSEL substrate. In **Fig. 4.2**, one such artifact

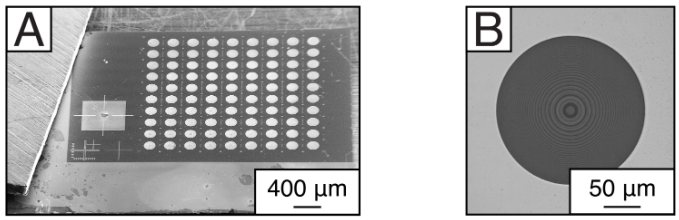

Figure 4.1: A) SEM image of the substrate side (or the metasurface side) of an MS-VCSEL chip with 81 individually addressable VCSELs, each with its own monolithically integrated metasurface. **B)** Microscope image of a monolithically integrated metasurface on the substrate side of the MS-VCSEL.

is presented for a dynamic-phase metasurface designed to focus and deflect the VCSEL beam. The focal length is set to compensate for the VCSEL divergence and focus the emitted beam $L_\mathrm{f} = 500$ µm away from the substrate, with a deflection angle of $\Theta_x = 15°$. The metaatoms are cylinders with a target height of $h = 700$ nm that discretize the 0–2π range in eight equal steps[1]. In **Fig. 4.2A**, a cross-section of a captured z-stack for the imaged emitted beam is presented, and, as seen, the light is split into two beams. One main beam acquires the designed phase profile, which is then deflected and focused according to the designed phase profile of the metasurface. However, the VCSEL beam is also split into an unintended second beam, deflected to roughly half the designed deflection angle ($\Theta_x \approx 7.5°$). The splitting into two beams is attributed to ARDE, which alters the designed phase profile of the fabricated metasurface. Either ARDE introduces a larger periodicity in the phase profile, which opens up diffraction orders, or ARDE increases the phase gradient such that the sampling rate is insufficient and the observed artifact is aliasing of the phase profile. The inset of the integrated line profile at the designed focal plane ($L_\mathrm{f} = 500$ µm) shows a spot size of $d_\mathrm{f} = 10.3$ µm, measured with the $1/e^2$-width.

To mitigate ARDE for dynamic-phase metasurfaces, it is advantageous to utilize a shallower etch depth ($h = 500$ nm) and a reduced phase

[1]The dimensions and complex transmission coefficient of these metaatoms are seen in **Fig. 3.11B-C**. The eight metaatoms are the cylinders marked in the figure.

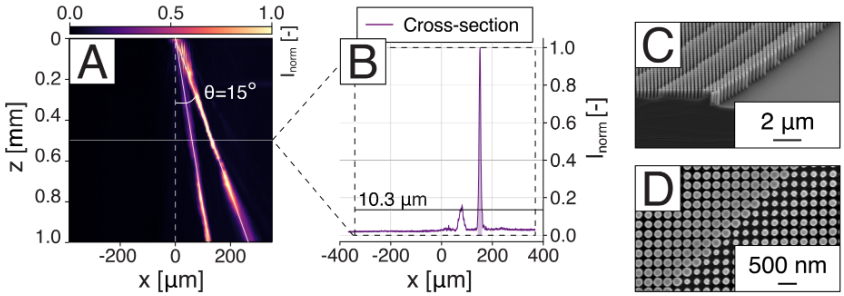

Figure 4.2: **A)** z-stack of the cross-section beam emitted by the VCSEL integrated with a dynamic-phase metasurface designed to focus the emitted beam to $L_\mathrm{f} = 600\,\mu\mathrm{m}$ and deflect the beam by $\Theta_x = 15°$. **B)** Cross-section of the beam in the designed focal plane. **C)** SEM cross-section of a metasurface fabricated on a separate GaAs substrate. **D)** SEM image of the top view of the etched dynamic-phase metasurface.

discretization (five discrete steps)[2]. Although transmission is lower with this shallower etch depth (**Fig. 3.11**), ARDE is also less pronounced. In **Fig. 4.3A**, cross-sections of the captured z-stacks can be seen for the shallower-etched dynamic-phase metasurface[3], designed to collimate the VCSEL beam using a metalens with a hyperbolic phase profile (**Eq. 3.2**) with a focal length $f = 178\,\mu\mathrm{m}$. This focal length compensates for the divergent beam of the VCSEL after propagating through the 630 µm-thick GaAs substrate. The divergence angles of the emitted beam along both axes are $\theta_{\mathrm{div,x}} = 1.28°$ and $\theta_{\mathrm{div,y}} = 1.02°$, measured from the $1/e^2$-width of the collimated beam, as shown in **Fig. 4.3B**. The fixed propagation distance from the VCSEL cavity to the metasurface (630 µm) means that the emitted beam has a fixed width when it is incident on the metasurface (**Fig. 2.11C**). This implies that the integrated metalens has a limited NA, which in turn limits how well the emitted beam can be collimated. From Fourier optics simulations, the smallest divergence angle possible for the beam emitted by the fabricated MS-VCSEL with a GaAs substrate thickness of 630 µm is $\theta_{\mathrm{div}} = 0.8°$. In addition, since the metasurface does not deflect the beam, it is difficult to estimate the relative transmission

[2]Similar to the metasurfaces fabricated at Beijing University, where researchers working on MS-VCSELs have demonstrated highly efficient dynamic-phase devices even in the presence of ARDE [68].

[3]The five metaatoms have radii r=65, 86, 101, 115, 125 nm, which discretize the phase profile into five even steps between 0 and 2π.

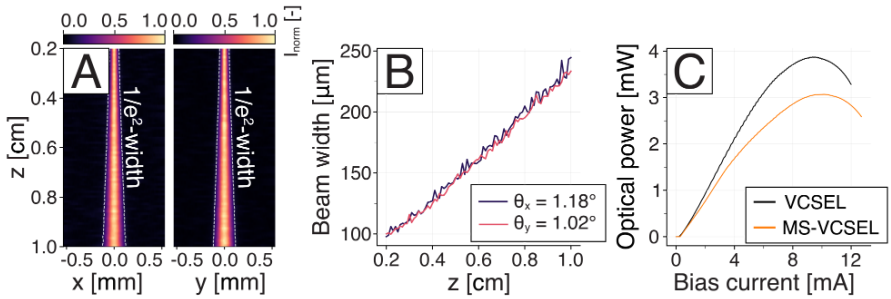

Figure 4.3: **A)** Cross-sections of the captured z-stack for both dimensions of the emitted VCSEL beam collimated by the dynamic-phase metasurface. **B)** The $1/e^2$-beam width of the collimated beam as a function of the propagation distance away from the VCSEL. **C)** IPV curve for the monolithically integrated VCSEL ($d_{\mathrm{ox}} = 3$ µm) with the dynamic-phase metasurface.

(η_r) from Fourier imaging alone. As mentioned, without a deflection angle to spatially separate them in the Fourier image, it is challenging to distinguish the untransformed light from the light that acquires the designed phase profile. However, in **Fig. 4.3C**, the IPV curve of the collimated beam was captured by a PD at a significant distance away from the substrate ($z_{\mathrm{sub}} > 2$ cm) and compared to the IPV of a VCSEL with a similarly sized aperture (d_{ox}) but without an integrated metasurface. Since light that is untransformed by the metasurface should retain the VCSEL divergence, most of the unmodulated light has diverged significantly at this distance. This comparison gives a rough estimate of the relative transmission efficiency of $\eta_r \approx 70 - 80\%$. More importantly, it verifies that metasurface integration does not significantly degrade the VCSEL performance in terms of threshold current and thermal rollover.

4.2 Geometric-phase MS-VCSELs

Geometric-phase metasurfaces worked efficiently and without optical artifacts under the ARDE constraint. This is attributed to the metasurface utilizing a single half-waveplate nanofin geometry across the entire structure. As the nanofins rotate to impart the geometric phase, the rotation changes the gaps between them, but it does so uniformly across the metasurface, which is believed to average out the ARDE. In

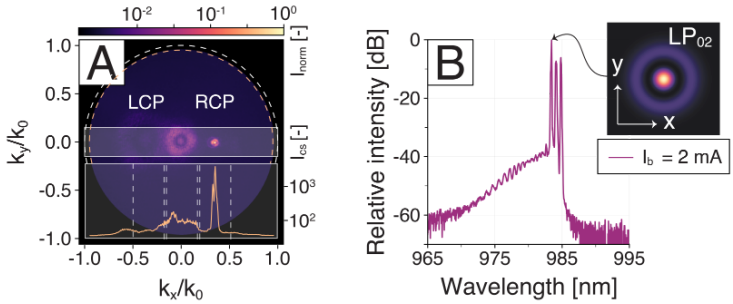

Figure 4.4: A) Fourier image of the integrated geometric phase metasurface. **B)** Spectrum as a VCSEL with a similarly sized oxide aperture ($d_{\text{ox}} = 4.8$ µm), where the presence of the higher-order mode changes the beam profile seen in the Fourier image.

Fig. 4.4A, a Fourier image is shown for a monolithically integrated geometric-phase metasurface. The metasurface is designed to collimate ($f = 630$ µm) and deflect ($\Theta_x = 20°$) the RCP component of the emitted VCSEL beam[4]. Since the linearly polarized beam from the VCSEL contains both RCP and LCP components, the LCP component is imparted with the opposite phase gradient, corresponding to a divergent lens ($f = -630$ µm) and a deflection angle ($\Theta_x = -20°$). As seen in the image, the RCP state is successfully collimated and deflected, displaying a narrow spread and a discrete shift ($k/k_0 = 0.34$) in the plane-wave spectrum. The LCP state is barely visible in **Fig. 4.4A**, as the corresponding divergent lens profile spreads it across the plane-wave spectrum. In the integrated cross-section, the LCP beam is barely visible as a small bump to the left of the untransformed light. In addition, this geometric-phase metasurface was integrated with a VCSEL featuring a larger aperture ($d_{\text{ox}} = 4.2$ µm). The presence of higher-order modes in the larger-aperture VCSEL is evident in the intensity profile in the Fourier image for both the modulated and unmodulated beams, which exhibit the shape of the LP$_{02}$ mode.

[4]The nanofins of the geometric-phase metasurface have widths $w_x = 202$ nm, $w_y = 91$ nm, and a height $h = 1000$ nm. The same design as in **Fig. 3.20D**. The complex transmission coefficients for this nanofin are shown in **Fig. 3.7D**.

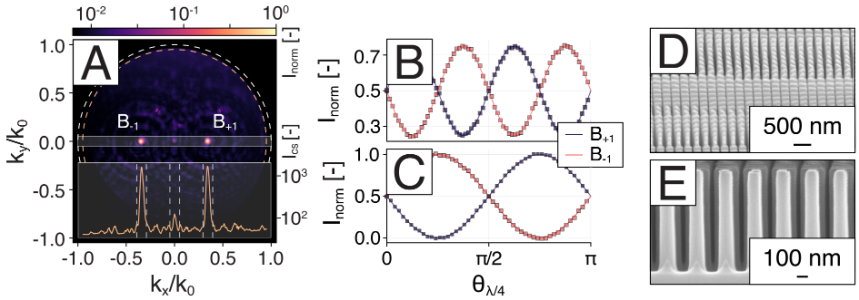

Figure 4.5: **A)** Fourier image of the emitted beam from the APM-VCSEL. Two clear Gaussian profiles are visible at deflection angles corresponding to $\Theta_x = \pm 20°$. **B)** Stokes parameter measurements for both deflected beams when the APM is integrated with a free-running VCSEL, and **C)** when it is integrated with a polarization-pinned VCSEL. **D)** SEM image of a tilted view and **E)** a cross-section of the fabricated APM.

4.3 Arbitrary polarization metasurface MS-VCSELs

The monolithically integrated APM worked with remarkably high efficiency despite the constraints of ARDE[5]. This excellent performance is attributed to the varied sizes and distribution of in-plane rotations across the metasurface, which effectively average out the ARDE. **Fig. 4.5A** presents a Fourier image of the VCSEL with an APM designed to collimate the emitted beam ($f = 630$ µm) and split the RCP and LCP constituents by deflecting them ($\Theta_x = \pm 20°$). Integration over the different areas in the image results in remarkably high relative transmission efficiency ($\eta_r > 90\%$).

However, while the phase profile of the APM successfully shapes the beam as designed, the emitted beams exhibit an anomaly in the polarization state when integrated with a free-running VCSEL, with the mode-hopping polarization from **Fig. 2.8A**. In **Fig. 4.5B**, the measurement of the Stokes parameters for each diffraction order in free space is shown using the rotating QWP technique [152]. The Stokes parameters of the two beams are $S_{B+1} = [1, 0, 1, 0]$ and $S_{B-1} = [1, 0, -1, 0]$ within the measurement errors, as presented in **Fig. 3.19B-C**, where the reference axis of the measurement is taken as close as possible

[5]The dimensions of the used metaatoms can be seen in **Fig. 3.7C**.

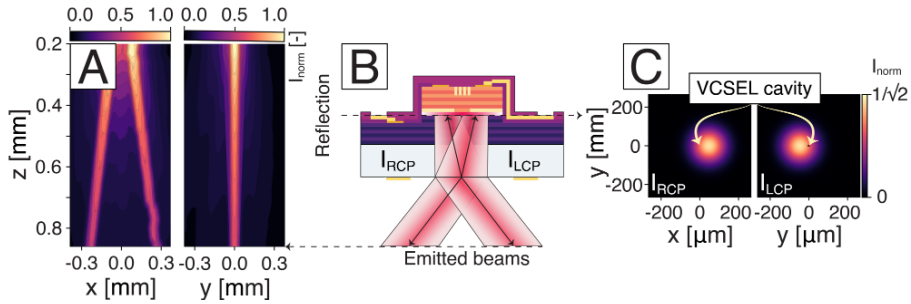

Figure 4.6: **A)** Cross-sections of the z-stacks of near-field of the monolithically integrated APM. **B)** The reflection from the APM splits the beam into two. One beam with a RCP state and one beam with a LCP state. **C)** Numerically propagated reflection from the APM, back to the plane of the VCSEL cavity.

to the $[0\bar{1}1]$-crystallographic axis of the GaAs substrate. So, the polarization states of the split beams are orthogonal to each other, but they are linear states oriented at an angle close to $\pm 45°$ from the major crystallographic axes of the GaAs substrate. In contrast, when the APM is passively illuminated by an external DFB laser with a well-defined polarization state, the outgoing split beams exhibit the correctly designed polarization states, as seen in **Fig. 3.17A**. Furthermore, when the APM is monolithically integrated into the substrate of a VCSEL with a subwavelength grating to pin the polarization state (**Fig. 2.13**), the polarization states of the beams are correctly split into the intended RCP and LCP states, as shown in **Fig. 4.5C**, with the measured Stokes parameters, $S_{B+1} = [1, 0, 0, 1]$ and $S_{B-1} = [1, 0, 0, -1]$ within the measurement errors. **Fig. 4.5D** displays a tilted SEM view of the fabricated APM, alongside a cross-section of the nanofins in **Fig. 4.5E**. Finally, **Fig. 4.6A** presents the captured near-field of the split beams as z-stacks, including cross-sections for both transverse dimensions.

Because the APM behaves as intended when illuminated by a stable, known polarization state, and the anomaly is only observed with the free-running VCSEL, I hypothesize that the anomaly stems from optical feedback from the metasurface back into the laser cavity. However, Fourier optics simulations utilizing the designed Jones matrices ($\mathbf{J}_{\mathrm{APM}}(x, y)$) indicate that there is no polarization of the incident beam (E_{in}) that produces the observed linear output. Regardless of the input polarization state, the geometric phase imparted by the rotation

of the half-waveplate nanofins should split the RCP component into one beam and the LCP component into the other. Altering the initial polarization state only determines the power distribution between the two transmitted beams (B_{+1} and B_{-1}), which depends only on how much power each component has in the initial state. Since there should only be RCP or LCP in each of the beams, there is no way to combine them to create a linear polarization state. However, Fourier optics simulations do not include near-field interactions or cross-coupling between adjacent metaatoms that could alter the designed function. To test this, full-wave simulations are performed with multiple metaatoms, using the APM as a blazed grating with five metaatoms. The same full-wave simulation is shown in **Fig. 3.13**, but with the APM metaatoms. These full-wave simulations confirmed the APM theory that the transmitted beam should split into RCP and LCP components.

Therefore, the anomaly is hypothesized to originate from polarization-dependent optical feedback. As schematically shown in **Fig. 4.6B**, the phase profile of the APM has a similar function in reflection, but with modified functionality (**Fig. 3.2**) since the reflected beam now propagates into the higher-refractive-index GaAs ($n_{\mathrm{GaAs}} = 3.52$). This implies that the imparted geometric phase should split the reflected beam into RCP and LCP states and deflect them by a smaller angle. Furthermore, the curvature of the hyperbolic phase profile used to collimate the beams is modified by the higher refractive index (**Eq. 3.2**). The higher refractive index means the APM focal length does not compensate for the VCSEL divergence in the reflection, and as a result the beams should continue to diverge in reflection. In **Fig. 4.6C**, the reflected field has been numerically propagated by Fourier optics back to the plane of the VCSEL cavity. As shown, both the reflected RCP and LCP beams overlap with the VCSEL cavity. It should be noted, however, that the Fourier simulations assume the medium from the metasurface back to the cavity is homogeneous GaAs. Nevertheless, for a free-running VCSEL, which lacks the anisotropy to pin the lasing to a certain crystallographic axis, this overlap from the reflection could pin the VCSEL to lase in a state that creates the observed $\pm 45^\circ$ linearly polarized beams. In addition, other demonstrated MS-VCSELs have monolithically integrated APMs [73]. However, they have not reported observing this polarization-state anomaly. However, their MS-VCSELs are grown on an n-doped GaAs substrate, which introduces significant

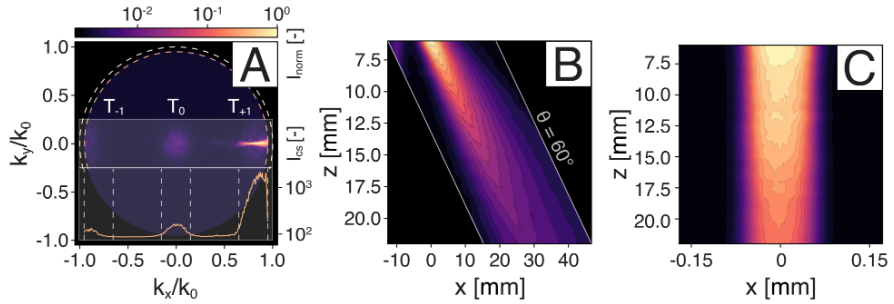

Figure 4.7: **A)** Fourier image of the VCSEL with an integrated offset-axicon metasurface. **B)** x-cross-section and **C)** y-cross-section of a captured z-stack for the fan-shaped beam of light.

free-carrier absorption as light propagates through the bottom substrate. This would heavily attenuate any optical feedback coupling back into the VCSEL cavity.

4.4 Offset-axicon MS-VCSELs

Since superunit-cell metasurfaces can be optimized with all gaps of equal width, ARDE can be effectively circumvented, resulting in high fabrication fidelity when integrated into the VCSEL substrate. In **Fig. 4.7A**, the Fourier image of the emitted beam from the integrated offset-axicon is presented, using the same metasurface as shown in **Fig. 3.21**. The elongated spectrum for the first diffraction order (T_{+1}) close to the NA of the objective corresponds to a fan-shaped beam of light. The shift seen along the x-axis is the deflection angle set by the diffractive period of the grating ($a_\mathrm{d} = 1136$ nm). The spread in the plane-wave spectrum along the x-axis corresponds to the maintained divergence of the VCSEL. Along the y-axis, the spectrum is compressed by the offset ($x_0 = 240$ µm) or the grating curvature, which is set to compensate for the divergence of the VCSEL. The fan-shaped beam was also imaged in free space, and x- and y-cross-sections of the captured z-stacks are presented in **Fig. 4.7B** and **Fig. 4.7C**, respectively. In **Fig. 4.7B**, the beam is deflected to the target angle ($\Theta_x = 60°$), and the divergence of the VCSEL along the x-axis is maintained as the beam continues to spread out. In **Fig. 4.7**, the collimation along the y-axis is seen as the beam is well collimated. The beam has a divergence angle of $\theta_{\mathrm{div,y}} = 0.92°$ from

the offset of the axicon. I refer to this as a fan-shaped beam because its beam shape resembles a hand fan: narrow in one dimension while spreading out in the other.

Chapter 5

Miniature integrated biophotonics

This final chapter discusses the utilization of MS-VCSELs as a platform for miniaturized biophotonics, which forms the core subject of two of the appended papers. Specifically, MS-VCSELs featuring an integrated offset-axicon were used to realize miniaturized illumination modules for two standard analytical techniques commonly utilized in biophotonics laboratories: high-contrast microscopy and surface plasmon resonance (SPR) sensing. Integrating both the optics and the light source onto a single semiconductor chip could enable the deployment of sensing technologies in novel, constrained environments. Furthermore, since each individual VCSEL can be equipped with its own unique metasurface, a single MS-VCSEL chip could simultaneously generate several tailored beams, either performing distinct tasks or designed to operate together for novel functionality. Finally, the chapter concludes with a discussion of our work on optical tweezers using an array of MS-VCSELs.

5.1 Miniaturized biophotonics with MS-VCSELs

Biophotonics is an interdisciplinary field that combines biology and photonics to explore and manipulate biological systems using light. Advanced tools, such as fluorescence microscopy [155], super-resolution microscopy [156–158], optical coherence tomography [159], and optical tweezers [160], provide insights by visualizing the otherwise unseen. Biophotonics is crucial for medical diagnostics, disease treatment, and fundamental research [161] by enabling the monitoring of molecular and

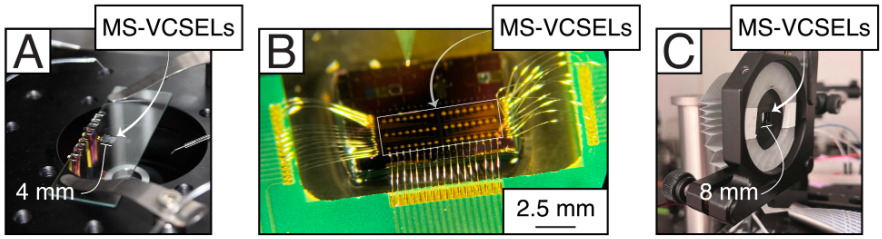

Figure 5.1: **A)** MS-VCSEL chip bonded to a glass substrate. The bonded 0.4×0.5 cm^2 chip contains 81 offset-axicon MS-VCSELs wire-bonded for current injection. **B)** Microscope image of the fan-out chip for wire-bonding with 3×16 MS-VCSELs. **C)** Mounted fan-out MS-VCSEL chip with metalenses for collimation of the emitted beams.

cellular processes. Driven by an ever-growing curiosity to image and probe novel biological phenomena, a large array of different biophotonic techniques and devices has been developed in recent decades [162]. The small device size of the MS-VCSEL could be utilized to miniaturize the illumination needed for several of the above-mentioned instruments. In **Fig. 5.1**, three such miniaturized illumination modules are shown, two of which have been utilized for the appended papers. These biophotonic techniques rely on specific properties of the illumination source, such as certain wavelengths, beam shapes, or polarization states, to enable accurate sensing. Since the MS-VCSEL can produce the needed beam directly on-chip, it could eliminate external optical elements, reducing the overall device size and time-consuming alignment. However, as discussed in previous chapters, the VCSEL produces a spontaneous-emission background (**Fig. 2.11A**) beyond the lasing peak, and fabricating a metasurface with 100% efficiency is very difficult. This means that in a fully integrated MS-VCSEL device, there is little room for using spatial or spectral filters to remove this unwanted light without reintroducing some of the bulky optics it would be designed to eliminate.

Nevertheless, the MS-VCSEL could bring advanced biophotonics into new environments by providing, for example, compact illumination for point-of-care diagnostics [163, 164]. Additionally, because the MS-VCSEL is a semiconductor laser, individual units could become highly cost-effective through economies of scale. This could unlock affordable

instrumentation for applications such as at-home healthcare [165, 166] and under-resourced laboratories. Furthermore, because each MS-VCSEL on a chip can be patterned with its own metasurface, a single chip can simultaneously emit several different beams for multiplexed sensing, or the beams can be combined to work in tandem. The ability to densely pack this level of optical functionality makes the MS-VCSEL a candidate light source to be integrated with microfluidic systems for a lab-on-a-chip device [167–169]. Our contribution has been to realize two such miniaturized illumination modules. A combined illumination source for high-contrast microscopy in dark-field (DF) and total internal reflection (TIR) modes, and an illumination source for angle-resolved surface plasmon resonance (SPR) sensing.

5.2 Dark-field and total internal reflection microscopy

Both DF and TIR illumination eliminate direct light from the illumination source, significantly improving the signal-to-noise ratio in the captured image. In DF microscopy, the light source is partially blocked, allowing only light with angles greater than the numerical aperture of the collection objective to illuminate the sample, as schematically shown in **Fig. 5.2A**. Because the direct light from the source is completely removed, the captured image consists only of light scattered by the sample. For TIR, the sample is illuminated by light incident at an angle greater than the critical angle at a sample interface, reflecting all light by total internal reflection. However, because an evanescent field extends beyond the reflecting interface, light can scatter from parts of the sample close to the surface, within the extent of the evanescent field ($\approx$ hundreds of nm).

The MS-VCSEL with an integrated offset-axicon metagrating can directly emit a fan-shaped beam (**Fig. 4.7**) into a glass environment, which can be used for both TIR and DF microscopy. The offset-axicon metagrating was optimized for emission into glass ($n_{\mathrm{glass}} = 1.51$) with a diffractive period ($a_{\mathrm{d}} = 730$ nm) to produce the fan-shaped beam centered around the critical angle between glass and air ($\theta_{\mathrm{TIR}} = 63°$). For both DF and TIR illumination, as shown in **Fig. 5.2B**, the MS-VCSEL arrays were bonded to a microscopy slide with a refractive-index-matched optical adhesive, emitting the beam directly into the

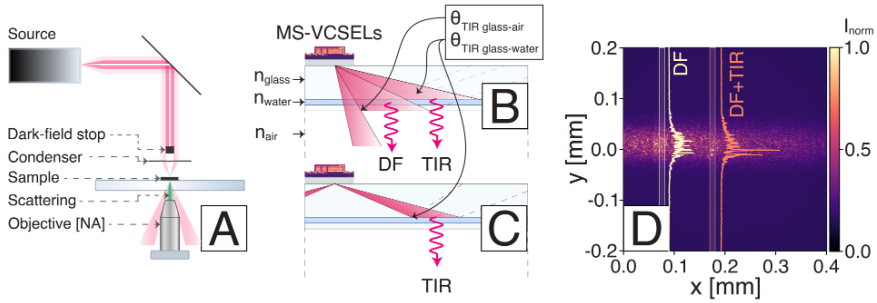

Figure 5.2: A) Schematic setup for DF microscopy. **B)** The DF illumination modes with the bonded MS-VCSEL array and **C)** the TIR illumination mode. **D)** Acquired DF-TIR image from a solution with gold nanorods. The first line section shows only scattered light from gold nanorods in the solution (DF). In the second line section, at least two rods are in close proximity to or stuck to the first glass-water interface, which significantly amplifies their scattering intensity, since they are within the exponential decay length of the evanescent field (TIR).

slide to illuminate a sample on the other side. The illumination angle from the offset-axicon metagrating is centered at $\Theta_x = 63°$, but spans the angular range of 30°–90°, as seen in **Fig. 4.7**. As shown in **Fig. 5.2B**, this means most of the light emitted from the MS-VCSEL is above the critical angle of the first glass-air interface ($\Theta_{\text{TIR,glass-air}} = 41.5°$) at the bottom of the stack. Additionally, to capture only the TIR-scattered light, a second type of metagrating was fabricated, where the offset-axicon is divided into two mirror-symmetric halves that deflect the emitted beam from the VCSEL to either $\Theta_x = \pm 63°$ [145]. This means that all light below $\Theta_x = 63°$ for either beam is deflected in the opposite direction. As a result, the sample can be illuminated using only light above the critical angle of the first glass-water interface ($\Theta_{\text{TIR,glass-water}} = 61°$), as schematically shown in **Fig. 5.2C**. In **Fig. 5.2D**, an image from the combined DF and TIR illumination (**Fig. 5.2B**) is shown for dissolved gold nanorods. The line of light corresponds to a single offset-axicon MS-VCSEL. Most of the light undergoes total internal reflection at the glass-air interface at the bottom of the stack (**Fig. 5.2B**). However, because the sample solution contains nanorods, the objective captures scattering from the particles (DF). Because the entire volume of the sample contributes to the signal, the integrated line section of the DF signal at $x = 0.08$ mm in **Fig. 5.2D** appears as a broad, Gaussian-like curve where individual

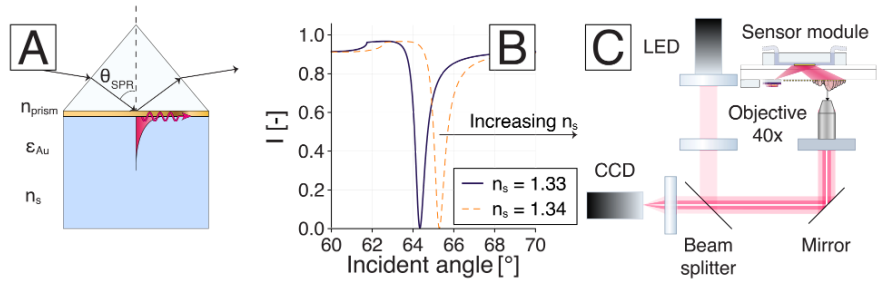

Figure 5.3: A) Excitation of SPP in the Kretschmann configuration along a thin gold film. **B)** Calculated theoretical reflection distribution for two different sensed refractive indices (n_s).**C)** Miniaturized illumination module setup for angle-resolved SPR sensing.

particles cannot be resolved. In contrast, the integrated line section at $x = 0.18$ mm shows a combined DF and TIR signal. Here, the scattering from all nanorods in the solution creates the broad background again, but the scattering intensity is significantly amplified for at least two specific particles. This enhancement occurs because these rods are either in close proximity to or stuck directly onto the first glass-water interface, placing them within the exponential decay length of the evanescent field.

5.3 Surface plasmon resonance

The same MS-VCSEL with the offset-axicon metagrating design was repurposed to enable a planar and miniaturized excitation module for surface plasmon polariton (SPP) excitation [170, 171]. Light propagates as a wave in free space by the coupling between the electric and magnetic fields. Because of the collective oscillations of free electrons in the metal, a metal can also couple to the electric field. Thus, a solution exists in which a bound wave propagates along a metal-dielectric interface, called an SPP. To excite the SPP, momentum matching[1] is required between an incident beam on the metal-dielectric interface and the surface mode. However, since the momentum of the SPP exceeds the largest possible in-plane momentum of light propagating in free space, an additional in-plane momentum must be supplied to the incident beam. This is most

[1]Here is a switch in the terminology from wave vectors and angles to momentum to align with standard SPP and SPR literature.

commonly done in what is called the Kretschmann configuration, as seen in **Fig. 5.3A**, where a prism with a higher refractive index (n_{prism}) is brought into contact with a thin metal film and illuminated at a steep angle [172]. With the larger refractive index, the incident wave can now reach a sufficiently large in-plane momentum to excite the SPP mode on the other side of the metal medium. By exciting the SPP in a thin film (usually a 50 nm Au film), the evanescent field extends beyond the metal. This creates a dependency of the momentum needed to excite the SPP on the refractive index within the evanescent field on the other side of the metal film as

$$\sin\theta_{\text{SPR}} = \frac{1}{n_{\text{prism}}}\sqrt{\frac{|\varepsilon_{\text{Au}}|n_{\text{s}}^2}{|\varepsilon_{\text{Au}}| - n_{\text{s}}^2}}, \tag{5.1}$$

where θ_{SPR} is the angle needed to excite the SPP, n_{prism} is the refractive index of the glass prism, ε_{Au} is the permittivity of the Au film, and n_{s} is the effective refractive index experienced by the evanescent field. Measuring changes to this coupling condition due to a refractive-index change is called surface plasmon resonance (SPR) sensing. For angle-resolved SPR, the thin Au film is illuminated over a broad angular range that covers the momentum-matching condition for the refractive-index range of interest, typically water ($n_{\text{s}} = 1.33$). As the incident beam illuminates the Au film, most of the light is reflected, except at the specific angles that are momentum-matched with the SPP. At these angles, the light is instead coupled into the surface mode and is thus not reflected. By capturing the reflected intensity distribution, an intensity dip can be found which corresponds to the angles that couple to the SPP. This is typically called the SPR dip, and its position in the reflected intensity distribution can be tracked to infer the momentum matching. In **Fig. 5.3B**, a calculated reflected intensity distribution (Fresnel multilayer theory [173]) can be seen as a function of the incident angle. With only water ($n_{\text{s}} = 1.33$) in the channel, the SPR dip is seen at $\Theta = 64.2°$, and as the refractive index within the evanescent field increases ($n_{\text{s}} = 1.34$), the SPR dip shifts to large angles.

Attempts at miniaturizing angle-resolved SPR sensing typically use the Kretschmann configuration and therefore rely on a bulky coupling prism to excite the SPP. In contrast, the MS-VCSEL with the offset-axicon metagrating can directly emit a beam into a glass environment with the required momentum, enabling the fabrication of a flat, integrable

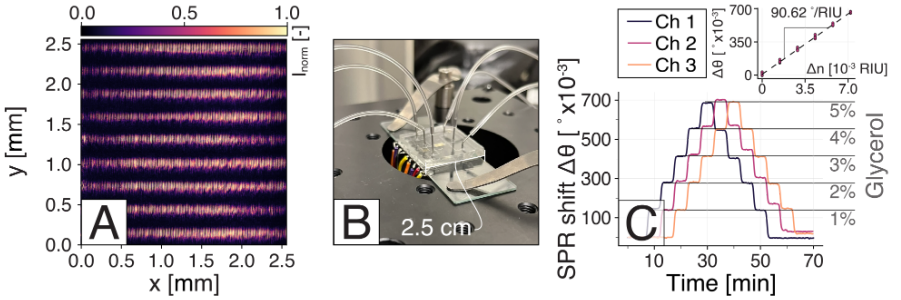

Figure 5.4: A) Nine VCSELs with offset-axicon metasurfaces outcoupled by the gold lines. All nine lasers could theoretically be used for measurements in nine independent channels. **B)** Captured reflectance distribution compared to the theoretical distribution. **C)** Calibration measurements for the bulk refractive index sensitivity of the miniature SPR sensor. Inset: The shift of the SRP dip in terms of the change in refractive index, or the sensor sensitivity ($\frac{\mathrm{d}\theta}{\mathrm{d}n} = 90.62°/\mathrm{RIU}$).

illumination module for SPP excitation. The demonstrated miniaturized illumination source is enabled by the MS-VCSEL with an integrated offset-axicon, meaning the prism can be eliminated entirely. The setup for the miniaturized illumination module for SPR is shown in **Fig. 5.3C**, where the array of MS-VCSELs is bonded to a 1.0 mm-thick glass slide using an index-matched optical adhesive. In the planar geometry, the angle of the SPP excitation is projected as

$$x = 2t_{\mathrm{glass}} \tan(\theta_{\mathrm{SPR}}), \tag{5.2}$$

where t_{glass} is the thickness of the glass slide to which the MS-VCSELs are bonded. This projection is special for the planar geometry and it implies that the sensitivity of the devices could be changed via the thickness of the glass slide (t_{glass}).

A complication of the planar geometry is that the angle of incidence for SPP excitation exceeds the critical angle at the outcoupling glass-air interface. This means the part of the beam with the intensity dip due to the SPP undergoes total internal reflection and is trapped inside the glass slide to which the MS-VCSELs are bonded. To couple light from the slide, Au strips (2 μm wide and spaced 15 μm apart) are patterned onto the top glass surface. The imaged outcoupling from the gold lines is shown for nine MS-VCSELs running in parallel in **Fig. 5.4A**. Furthermore, the MS-VCSEL illumination source is interfaced with a

polydimethylsiloxane (PDMS) microfluidic chip for analyte perfusion, as shown in **Fig. 5.4B**. The PDMS microfluidics were fabricated by deep reactive-ion etching of a Si master mold, followed by molding the microfluidics into a PDMS slab. The microfluidic layout has three channels of equal length and bend count, each with an individual inlet and outlet. This design keeps the pressure similar across all three sensing channels. The nine MS-VCSELs seen in **Fig. 5.4A** could measure the SPR shift from nine independent channels in parallel. However, I did not manage to fabricate such thin PDMS microfluidic channels without them leaking. All the demostrations where made with three independent channels, which could be extended by a better microfludics platform. The standard calibration curve for the SPR sensor involves bulk refractive index measurements, in which an analyte with an incrementally increasing refractive index is introduced into the sensing channel. In **Fig. 5.4C**, five different concentrations of glycerol (1–5%) in deionized water are measured in incremental steps across three independent channels. calibrating the bulk refractive index sensitivity of the miniaturized sensor. Because the refractive index of each glycerol solution is precisely known, it can be used to calibrate the SPR sensor sensitivity ($\frac{\mathrm{d}\theta}{\mathrm{d}n}$). The inset of **Fig. 5.4C** shows the angular shift of the SPR dip ($\Delta\theta$) as a function of the refractive-index change (Δn) across five different glycerol concentrations in repeated experiments. A linear fit to these data points yields the sensor sensitivity, defined as the angular shift per refractive index unit (RIU) [174].

5.4 Optical tweezing

Optical tweezing is a powerful biophotonic technique that utilizes the momentum of light to trap and manipulate microscopic particles. Pioneered by Arthur Ashkin and recognized with the 2018 Nobel Prize in Physics [175], optical tweezers have become an indispensable tool for probing cellular dynamics and molecular forces. Optical tweezers rely on the principle that a dielectric particle experiences a restoring force proportional to the intensity gradient in an optical field. When a laser beam is sharply focused, a potential forms at the focal point that can trap and manipulate microscopic particles [176]. While standard VCSEL arrays have been used as the light source to create optical traps [177–180], integrating metasurfaces directly into the substrate

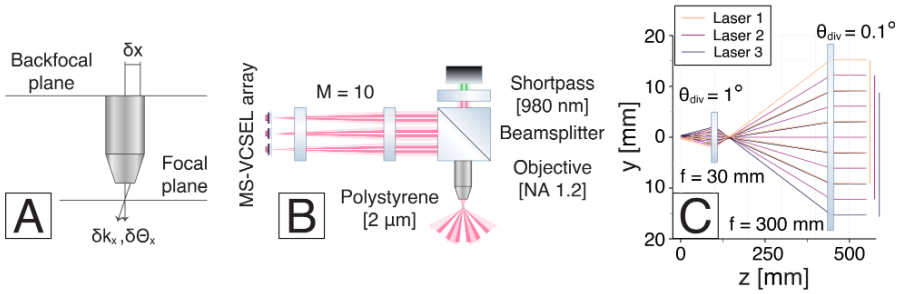

Figure 5.5: A) The focal plane of an objective is the Fourier transform of the intensity distribution at the back-focal plane. A ray incident off-center in the back-focal plane reaches the focal point at a larger angle, with higher in-plane momentum. **B)** Schematic setup for optical tweezing with the MS-VCSEL array. **C)** Ray tracing for the expansion of the MS-VCSEL beams. Magnifying the beams reduces their divergence angle. In addition, the larger beam fills the entire back-focal plane of the objective.

could offer a new degree of control over the potential in the focal plane.

The idea is that by illuminating the back-focal plane with individual spatially separated collimated beams from the MS-VCSELs, the intensity distribution in the back-focal plane of the objective can be controlled. The function of the objective, similar to Fourier imaging, is to transform the transverse intensity distribution in the back-focal plane into a distribution of in-plane momentum[2] in the focus. A ray at the center of the back-focal plane will propagate to the focus straight along the optical axis, as shown in **Fig. 5.5A**. In contrast, an off-center ray (δx) will still propagate to the same focal point, but at a steeper angle ($\delta\Theta_x$) and with a larger in-plane momentum (δk_x). Typically, to generate a stiff optical trap, the tweezing laser overfills the back-focal plane to create a uniform intensity distribution. With a dense array of individually addressable MS-VCSELs, the emitted beams from MS-VCSELs can be collimated by their respective metasurfaces and collectively focused by a high-NA objective, or potentially a secondary metasurface, to form the optical trap, schematically shown in **Fig. 5.5B**. Since each MS-VCSEL can be driven with an independent current, the intensity profile of the combined focus could be dynamically controlled. This enables electronic (non-mechanical) control of the

[2]Again momentum instead of angles or wave vectors.

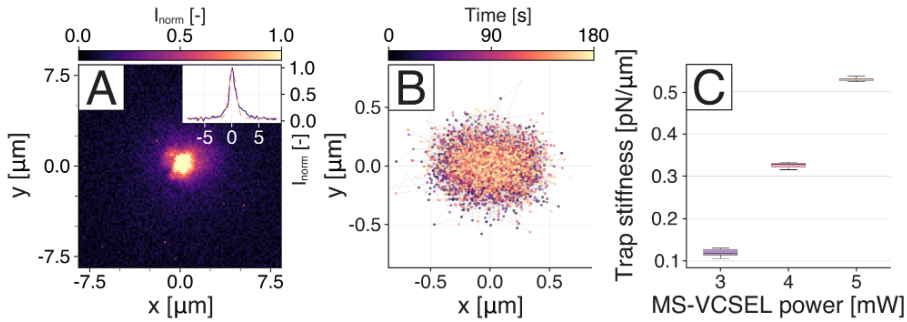

Figure 5.6: A) Spot size of a focused beam from the collimated MS-VCSEL array. The spot size is captured by illuminating a drop-cast layer of upconverting erbium-ytterbium particles. Inset: Line section of the spot size. The spot size is taken as the $1/e^2$-width from the Gaussian fit shown in the inset.**B)** Time trace for a trapped particle over 3 min, with MS-VCSEL output power of $P_{\text{out}} = 3$ mW. **C)** Trap stiffness (κ) as a function of the MS-VCSEL power measured ten separate times for every MS-VCSEL power.

intensity distribution at the back-focal plane and, in turn, the optical potential of the tweezer.

However, the limited divergence angle of the monolithically integrated metalenses, as seen in **Fig. 4.3**, is detrimental to creating a sharp focus with the MS-VCSELs. Although the achieved divergence angle, $\theta_{\text{div}} \approx 1°$, sounds fairly small, it limits the spot size of the focus created by the high-NA objective. Since the sharpest focus would be created with a plane-wave illuminating the back-focal plane, the slightly divergent MS-VCSEL beam did not create a sharp enough focus to trap a particle. This was mitigated by expanding ($M = 10$) the collimated beam, ray-traced in **Fig. 5.5C** for three MS-VCSELs, which both increased the illuminated area of the back-focal plane of the objective and reduced the divergence angle ($\theta_{\text{div}} = 0.1°$) of the beam incident on the back-focal plane. The resulting focal point from one MS-VCSEL is shown in **Fig. 5.6A**, where the inset line profile shows a spot size of $d_{\text{spot}} = 2.69$ µm, taken as the $1/e^2$-width of a Gaussian fit. This focus produced a strong enough optical potential to trap 2 µm polystyrene particles ($n_{\text{poly}} = 1.58$) in water ($n_{\text{water}} = 1.33$) with a single MS-VCSEL. A 3-minute time trace of a trapped polystyrene particle is shown in **Fig. 5.6B**, captured with an exposure time of 32 ms. The resulting trap stiffness was calculated from the position

variance of the time traces using the equipartition theorem [181][3], and is shown in **Fig. 5.6B** as a function of the MS-VCSEL output power. We measured the trap stiffness from ten time traces when trapping a polystyrene particle for 10 min at each VCSEL power.

However, the expansion necessary for producing the sharp focus for a single MS-VCSEL centered on the optical axis of the external optics caused the beam from a spatially offset MS-VCSEL to be incident on the back-focal plane at an angle. Since the offset beams are incident on the back-focal plane of the objective at an angle, the focal points of spatially offset MS-VCSELs do not overlap in the focal plane. Growing the VCSELs on a thicker GaAs substrate allows the beam width to expand before it reaches the metasurface. However, another significant problem is that the MS-VCSELs are not phase-locked. As such, the combined beams will not interfere constructively in the focal plane of the objective.

[3] $\kappa = \frac{k_b T}{\langle x \rangle^2}$, where κ is the trap stiffness, k_b is Boltzmann's constant, and $T = 22°$ is the assumed temperature in the trapped medium. $\langle x^2 \rangle$ is the measured variance of the position of the trapped particle.

Chapter 6

Future outlook

The monolithic integration of high-contrast dielectric metasurfaces with bottom-emitting VCSELs provides a compact, mechanically robust platform for generating tailored optical beams. These devices could miniaturize and integrate complex illumination sources for a variety of applications. While aspect-ratio-dependent etching (ARDE) remains the primary fabrication challenge, future iterations could address it by depositing high-contrast dielectric materials on the substrate surface to provide a dedicated etch-stop layer for metasurface fabrication. Alternatively, as demonstrated in this thesis, diffractive superunit cells and metagratings can effectively circumvent ARDE by utilizing uniform gap sizes. Furthermore, the fixed propagation distance from the VCSEL cavity to the metasurface limits the numerical aperture (NA) of any monolithically integrated metasurfaces. Future designs should consider the NA needed for the planned utilization of the MS-VCSELs. Another approach would be to integrate a metasurface on a separate substrate. While this maintains a relatively small device size, it compromises the robustness of fully monolithic integration and reintroduces an extra alignment step.

Beyond passive beam shaping, the anomaly observed in the polarization behavior of the monolithically integrated APMs hints at a coupling between the VCSEL and the metasurface. While currently an unsolved artifact, this feedback effect could potentially be utilized for future designs. By intentionally designing the metasurface to provide polarization- or spatial-mode-selective feedback, spatially tailored feedback from the metasurface could create an external cavity and enable

novel control of the lasing mode in the VCSEL. Finally, while the initial demonstrations in this work featured individual lasers or small arrays of independently addressable MS-VCSELs, there is significant potential in densely packing MS-VCSELs into larger arrays. If fabrication uniformity can be sufficiently maintained across larger areas, future efforts could explore MS-VCSEL arrays on a broader scale. Because each VCSEL can be monolithically integrated with a uniquely tailored metasurface, a single chip could either simultaneously execute several different optical functions or work in tandem for complex optical beam shaping.

Chapter 7

Summary of Papers

Paper A

Mindaugas Juodėnas, **Erik Strandberg**, Alexander Grabowski, Johan Gustavsson, Hana Jungová-Šipová, and Mikael Käll,
"High-angle deflection of metagrating-integrated laser emission for high-contrast microscopy",
Light: Science and Applications, vol. 12, no. 1, p. 251, 2023

We demonstrate a miniaturized illumination module for high-contrast microscopy, enabled by metasurface-integrated VCSELs (MS-VCSELs). The metasurfaces are offset-axicon metagrating that very efficiently deflect light to large angles along one dimension while simultaneously focusing light along the perpendicular dimension. When integrated with a VCSEL, it creates a thin fan-shaped beam at a steep angle that can be used for high-contrast microscopy. In addition, the supercell metagrating design can function very efficiently under the constraint that all gaps have uniform widths across the metasurface. This circumvents aspect-ratio-dependent etching inherent to etching without an etch-stop layer and allows for very high fabrication fidelity when etching into the pure GaAs substrate of the VCSEL. We fabricated the MS-VCSELs with two types of metagrating to support two different high-contrast illumination modes: dark-field and total-internal reflection. By integrating two MS-VCSELs dedicated to the two modes in close proximity (200 µm) on the same chip, enabling rapid (electronic) switching between the two high-contrast illumination modes for the same sample.

My contributions: Design and fabrication of the single-mode bottom-emitting VCSELs. Characterization of the standalone VCSELs and the integrated MS-VCSELs, and analysis of the data. Co-wrote the initial draft for the paper and revised the paper with feedback from reviewers.

Paper B

Erik Strandberg, Mindaugas Juodėnas, Hana Jungová-Šipová, and Mikael Käll,
"Flat Plasmonic Biosensor with an On-Chip Metagrating-Integrated Laser",
ACS: Sensors, vol. 10, no. 10, pp. 7670–7678, 2025
We demonstrate a miniaturized illumination module for angle-resolved surface plasmon resonance (SPR) sensing, enabled by metasurface-integrated VCSELs (MS-VCSELs). By repurposing the offset-axicon metagrating design, the emitted fan-shaped beam is deflected to the angle required to excite surface plasmon polaritons along a thin gold film. This approach realizes SPR sensing in a new compact, integrable, and flat format. In addition, by bonding the MS-VCSELs to a glass substrate equipped with polydimethylsiloxane (PDMS) microfluidic channels, we enabled independent, parallel SPR measurements across multiple channels. Characterization of both the bulk and surface sensitivity of the miniaturized sensor demonstrated a sensitivity of $4.9 \cdot 10^{-1}$ refractive index units (RIU). Finally, the practical sensing capability of the device was validated through a proof-of-concept microRNA assay, achieving a direct detection limit of 0.1 nM and an antibody-amplified limit of 0.02 nM for the liver disease-associated biomarker microRNA-122 (miR-122).
My contributions: Design, fabrication, and characterization of the MS-VCSELs for surface-plasmon excitation. Packaging of the MS-VCSEL chips, as well as fabrication of the gold-coated excitation slides and the PDMS microfluidics. Measured the SPR sensor characterization and the biosensing experiments. I co-wrote the initial draft, implemented feedback from co-authors, and revised the manuscript with feedback from reviewers

Paper C

Erik Strandberg, Mindaugas Juodėnas, Alexander Grabowski, Åsa Haglund, and Anders Larsson,

"Buried Subwavelength Gratings for Polarization Pinning of Bottom-Emitting GaAs VCSELs",
IEEE: Selected Topics on Quantum Electronics, vol. 32, no. 6, pp. 1701408–1701408, 2026.
We demonstrate the pinning of the inherently unpredictable polarization state in bottom-emitting GaAs VCSELs with circular oxide apertures by integrating a subwavelength grating directly into the highly reflective top distributed Bragg reflector (DBR). The subwavelength grating creates anisotropic reflections from the top DBR that can suppress lasing along either of the major crystallographic axes of the GaAs substrate. In addition, the grating can pin the polarization while it is buried beneath a SiN_x film, protecting it from further fabrication, such as monolithic integration of a metasurface on the substrate side. The buried grating successfully pins the polarization for aperture diameters up to 4 µm, and the 3 µm aperture VCSELs achieve single-mode, single-polarization operation, delivering 3.9 mW of output power with a side-mode suppression ratio exceeding 30 dB and an orthogonal polarization suppression ratio (OPSR) of 20 dB.
My contributions: Design and fabrication of the bottom-emitting VCSELs with integrated subwavelength gratings for polarization pinning. Characterization of the polarization pinning in the VCSELs. Wrote the initial draft, implemented feedback for co-authors, and revised the manuscript with feedback from reviewers.

References

[1] J. P. Gordon, H. J. Zeiger, and C. H. Townes, "The Maser—New Type of Microwave Amplifier, Frequency Standard, and Spectrometer," *Physical Review*, vol. 99, no. 4, pp. 1264–1274, 1955.

[2] T. H. Maiman, "Stimulated Optical Radiation in Ruby," *Nature*, vol. 187, no. 4736, pp. 493–494, 1960.

[3] A. Javan, W. R. Bennett, and D. R. Herriott, "Population Inversion and Continuous Optical Maser Oscillation in a Gas Discharge Containing a He-Ne Mixture," *Physical Review Letters*, vol. 6, no. 3, pp. 106–110, 1961.

[4] L. A. Coldren, S. W. Corzine, and M. L. Mašanović, *Diode Lasers and Photonic Integrated Circuits*, 1st ed. Wiley, 2012.

[5] Y.-C. Chang and L. A. Coldren, "Design and Performance of High-Speed VCSELs," in *VCSELs*, R. Michalzik, Ed. Berlin, Heidelberg: Springer Berlin Heidelberg, 2013, vol. 166, pp. 233–262, springer Series in Optical Sciences.

[6] R. Jäger, M. Grabherr, C. Jung, R. Michalzik, G. Reiner, B. Weigl, and K. Ebeling, "57% wallplug efficiency oxide-confined 850 nm wavelengthGaAs VCSELs," *Electronics Letters*, vol. 33, no. 4, pp. 330–331, 1997.

[7] L. Wang, H. Qu, A. Qi, X. Zhou, and W. Zheng, "High-power laser diode at 9xx nm with 81.10% efficiency," *Optics Letters*, vol. 47, no. 13, p. 3231, 2022.

[8] K. Iga, "Surface-emitting laser-its birth and generation of new optoelectronics field," *IEEE Journal of Selected Topics in Quantum Electronics*, vol. 6, no. 6, pp. 1201–1215, 2000.

[9] W. Brinkman, D. Haggan, and W. Troutman, "A history of the invention of the transistor and where it will lead us," *IEEE Journal of Solid-State Circuits*, vol. 32, no. 12, pp. 1858–1865, 1997.

[10] K. Choquette and H. Hou, "Vertical-cavity surface emitting lasers: moving from research to manufacturing," *Proceedings of the IEEE*, vol. 85, no. 11, pp. 1730–1739, 1997.

[11] G. P. Agrawal and N. K. Dutta, *Semiconductor Lasers*, 2nd ed. Boston, MA: Springer US, 1993.

[12] R. N. Hall, G. E. Fenner, J. D. Kingsley, T. J. Soltys, and R. O. Carlson, "Coherent Light Emission From GaAs Junctions," *Physical Review Letters*, vol. 9, no. 9, pp. 366–368, 1962.

[13] J. Jewell, A. Scherer, B. Van Der Gaag, L. Schiavone, J. Harbison, and L. Florez, "Microcavity VCSELs," *Quantum Optoelectronics*. Optica Publishing Group, 1993, p. QThA.1.

[14] K. Lear, K. Choquette, R. Schneider, S. Kilcoyne, and K. Geib, "Selectively oxidised vertical cavity surface emitting lasers with 50% power conversion efficiency," *Electronics Letters*, vol. 31, no. 3, pp. 208–209, 1995.

[15] P. Westbergh, J. Gustavsson, A. Haglund, M. Skold, A. Joel, and A. Larsson, "High-Speed, Low-Current-Density 850 nm VCSELs," *IEEE Journal of Selected Topics in Quantum Electronics*, vol. 15, no. 3, pp. 694–703, 2009.

[16] H.-T. Cheng, Y.-C. Yang, T.-H. Liu, and C.-H. Wu, "Recent Advances in 850 nm VCSELs for High-Speed Interconnects," *Photonics*, vol. 9, no. 2, p. 107, 2022.

[17] M. E. Warren, R. F. Carson, J. R. Joseph, T. Wilcox, P. Dacha, D. J. Abell, and K. J. Otis, "High-speed and scalable high-power VCSEL arrays and their applications," *High-speed and scalable high-power VCSEL arrays and their applications*, C. Lei and K. D. Choquette, Eds., San Francisco, California, United States, 2015, p. 93810C.

[18] H. Soda, K.-I. Iga, C. Kitahara, and Y. Suematsu, "GaInAsP/InP Surface Emitting Injection Lasers," *Japanese Journal of Applied Physics*, vol. 18, no. 12, pp. 2329–2330, 1979.

[19] K. Iga, "Vertical-Cavity Surface-Emitting Laser: Its Conception and Evolution," *Japanese Journal of Applied Physics*, vol. 47, no. 1R, p. 1, 2008.

[20] H. Dalir and F. Koyama, "High-speed operation of bow-tie-shaped oxide aperture VCSELs with photon–photon resonance," *Applied Physics Express*, vol. 7, no. 2, p. 022102, 2014.

[21] H. Lu, O. Alkhazragi, H. Lin, T. K. Ng, and B. S. Ooi, "Shaping the light of VCSELs through cavity geometry design," *Light: Science & Applications*, vol. 14, no. 1, p. 344, 2025.

[22] W. Yan, O. Alkhazragi, H. Lu, R. H. Al Ibrahim, Y. Wang, H. Lin, Y. Banda, G. Melinte, T. K. Ng, and B. S. Ooi, "Annular cavity VCSELs: enhanced beam quality and speckle-less illumination," *Optics Express*, vol. 33, no. 5, p. 9539, 2025.

[23] Y. Xiao, J. Wang, H. Liu, P. Miao, Y. Gou, Z. Zhang, G. Deng, and S. Zhou, "Multi-junction cascaded vertical-cavity surface-emitting laser with a high power conversion efficiency of 74%," *Light: Science & Applications*, vol. 13, no. 1, p. 60, 2024.

[24] V. Torrelli, A. Gullino, J. Lindner, G. Moiso, M. D'Alessandro, S. Gronenborn, M. Herper, T. Pusch, H. Moench, A. Tibaldi, F. Bertazzi, M. Goano, M. C. G. Alasio, and P. Debernardi, "Beyond 30 mW of Single-Mode Power in Linearly-Polarised VCSELs," *IEEE Journal of Selected Topics in Quantum Electronics*, vol. 32, no. 6: Special Issue on Advances in, pp. 1 701 012–1 701 012, 2026.

[25] P. Westbergh, R. Safaisini, E. Haglund, J. S. Gustavsson, A. Larsson, M. Geen, R. Lawrence, and A. Joel, "High-Speed Oxide Confined 850-nm VCSELs Operating Error-Free at 40 Gb/s up to 85°C," *IEEE Photonics Technology Letters*, vol. 25, no. 8, pp. 768–771, 2013.

[26] D. M. Kuchta, A. V. Rylyakov, C. L. Schow, J. E. Proesel, C. W. Baks, P. Westbergh, J. S. Gustavsson, and A. Larsson, "A 50 Gb/s NRZ Modulated 850 nm VCSEL Transmitter Operating Error Free to 90 °C," *Journal of Lightwave Technology*, vol. 33, no. 4, pp. 802–810, 2015.

[27] M. Grabherr, H. Moench, and A. Pruijmboom, "VCSELs for Optical Mice and Sensing," in *VCSELs*, R. Michalzik, Ed. Berlin, Heidelberg: Springer Berlin Heidelberg, 2013, vol. 166, pp. 521–538, series Title: Springer Series in Optical Sciences.

[28] D. K. Serkland, G. M. Peake, K. M. Geib, R. Lutwak, R. M. Garvey, M. Varghese, and M. Mescher, "VCSELs for atomic clocks," *VCSELs for atomic clocks*, C. Lei and K. D. Choquette, Eds., San Jose, CA, 2006, p. 613208.

[29] J. Lindner, T. Pusch, S. Gronenborn, J. Reichel, U. Weichmann, M. Herper, A. Van Der Lee, S. Weidenfeld, C. Klett, H. Moench, and R. A. Koerner, "Compact VCSEL chips for diverse applications (795 nm to 850 nm)," *Vertical-Cavity Surface-Emitting Lasers XXIX*, K. D. Choquette and L. A. Graham, Eds. San Francisco, United States: SPIE, 2025, p. 15.

[30] N. Mukoyama, H. Otoma, J. Sakurai, N. Ueki, and H. Nakayama, "VCSEL array-based light exposure system for laser printing," *VCSEL array-based light exposure system for laser printing*, C. Lei and J. K. Guenter, Eds., 2026, p. 69080H.

[31] B. Pesach, Z. Mor, S. Yalov, and A. Shpunt, "Projectors of structured light," U.S. patent 20 130 038 881A1, 2013.

[32] M. Dummer, K. Johnson, S. Rothwell, K. Tatah, and M. K. Hibbs-Brenner, "The role of VCSELs in 3D sensing and LiDAR," *Optical Interconnects XXI*, H. Schröder and R. T. Chen, Eds. SPIE, 2021, p. 9.

[33] C.-H. Cheng, C.-C. Shen, H.-Y. Kao, D.-H. Hsieh, H.-Y. Wang, Y.-W. Yeh, Y.-T. Lu, S.-W. Huang Chen, C.-T. Tsai, Y.-C. Chi, T. S. Kao, C.-H. Wu, H.-C. Kuo, P.-T. Lee, and G.-R. Lin, "850/940-nm VCSEL for optical communication and 3D sensing," *Opto-Electronic Advances*, vol. 1, no. 3, p. 180005, 2018.

[34] C. Zhang, H. Li, and D. Liang, "Antireflective vertical-cavity surface-emitting laser for LiDAR," *Nature Communications*, vol. 15, no. 1, p. 1105, 2024.

[35] Y. Liu and X. Zhang, "Metamaterials: a new frontier of science and technology," *Chemical Society Reviews*, vol. 40, no. 5, p. 2494, 2011.

[36] M. Kadic, G. W. Milton, M. Van Hecke, and M. Wegener, "3d metamaterials," *Nature Reviews Physics*, vol. 1, no. 3, pp. 198–210, 2019.

[37] J. B. Pendry, "Negative Refraction Makes a Perfect Lens," *Physical Review Letters*, vol. 85, no. 18, pp. 3966–3969, 2000.

[38] N. Kundtz and D. R. Smith, "Extreme-angle broadband metamaterial lens," *Nature Materials*, vol. 9, no. 2, pp. 129–132, 2010.

[39] T. J. Cui, R. Liu, and D. Smith, *Metamaterials: Theory, Design, and Applications*, ser. SpringerLink Bücher. Boston, MA: Springer US, 2010.

[40] N. Yu, P. Genevet, M. A. Kats, F. Aieta, J.-P. Tetienne, F. Capasso, and Z. Gaburro, "Light Propagation with Phase Discontinuities: Generalized Laws of Reflection and Refraction," *Science*, vol. 334, no. 6054, pp. 333–337, 2011.

[41] V. G. Veselago, "The Electrodynamics of Substances with Simultaneously Negative Values of ϵ and μ," *Soviet Physics Uspekhi*, vol. 10, no. 4, pp. 509–514, 1968.

[42] R. A. Shelby, D. R. Smith, and S. Schultz, "Experimental Verification of a Negative Index of Refraction," *Science*, vol. 292, no. 5514, pp. 77–79, 2001.

[43] P. Genevet, F. Capasso, F. Aieta, M. Khorasaninejad, and R. Devlin, "Recent advances in planar optics: from plasmonic to dielectric metasurfaces," *Optica*, vol. 4, no. 1, p. 139, 2017.

[44] K. Miyamoto, "The Phase Fresnel Lens," *Journal of the Optical Society of America*, vol. 51, no. 1, p. 17, 1961.

[45] G. J. Swanson, "Binary Optics Technology: The Theory and Design of Multi-Level Diffractive Optical Elements:," Defense Technical Information Center, Fort Belvoir, VA, Tech. Rep., 1989.

[46] J. Bengtsson, *Diffractive optics design*, ser. Technical report / School of Electrical and Computer Engineering, Chalmers University of Technology, Göteborg, Sweden. Göteborg: Chalmers tekniska högsk, 1997, no. 314.

[47] S. N. Khonina, N. L. Kazanskiy, R. V. Skidanov, and M. A. Butt, "Advancements and Applications of Diffractive Optical Elements in Contemporary Optics: A Comprehensive Overview," *Advanced Materials Technologies*, p. 2401028, 2024.

[48] I. Minin and O. Minin, *Diffractive Optics and Nanophotonics: Resolution Below the Diffraction Limit*, ser. SpringerBriefs in Physics. Cham: Springer International Publishing, 2016.

[49] H.-T. Chen, A. J. Taylor, and N. Yu, "A review of metasurfaces: physics and applications," *Reports on Progress in Physics*, vol. 79, no. 7, p. 076401, 2016.

[50] S. M. Kamali, E. Arbabi, A. Arbabi, and A. Faraon, "A review of dielectric optical metasurfaces for wavefront control," *Nanophotonics*, vol. 7, no. 6, pp. 1041–1068, 2018.

[51] N. A. Rubin, G. D'Aversa, P. Chevalier, Z. Shi, W. T. Chen, and F. Capasso, "Matrix Fourier optics enables a compact full-Stokes polarization camera," *Science*, vol. 365, no. 6448, p. eaax1839, 2019.

[52] Q. Fan, W. Xu, X. Hu, W. Zhu, T. Yue, F. Yan, P. Lin, L. Chen, J. Song, H. J. Lezec, A. Agrawal, Y. Lu, and T. Xu, "Disordered metasurface enabled single-shot full-Stokes polarization imaging leveraging weak dichroism," *Nature Communications*, vol. 14, no. 1, p. 7180, 2023.

[53] P. R. West, J. L. Stewart, A. V. Kildishev, V. M. Shalaev, V. V. Shkunov, F. Strohkendl, Y. A. Zakharenkov, R. K. Dodds, and R. Byren, "All-dielectric subwavelength metasurface focusing lens," *Optics Express*, vol. 22, no. 21, p. 26212, 2014.

[54] Z. Wang, T. Li, A. Soman, D. Mao, T. Kananen, and T. Gu, "On-chip wavefront shaping with dielectric metasurface," *Nature Communications*, vol. 10, no. 1, p. 3547, 2019.

[55] S. Gao, C. Park, S. Lee, and D. Choi, "A Highly Efficient Bifunctional Dielectric Metasurface Enabling Polarization-Tuned Focusing and Deflection for Visible Light," *Advanced Optical Materials*, vol. 7, no. 9, p. 1801337, 2019.

[56] Y. Hu, X. Wang, X. Luo, X. Ou, L. Li, Y. Chen, Ping Yang, S. Wang, and H. Duan, "All-dielectric metasurfaces for polarization manipulation: principles and emerging applications," *Nanophotonics*, vol. 9, no. 12, pp. 3755–3780, 2020.

[57] S. Chen, W. Liu, Z. Li, H. Cheng, and J. Tian, "Metasurface-Empowered Optical Multiplexing and Multifunction," *Advanced Materials*, vol. 32, no. 3, p. 1805912, 2020.

[58] R. C. Devlin, M. Khorasaninejad, W. T. Chen, J. Oh, and F. Capasso, "Broadband high-efficiency dielectric metasurfaces for the visible spectrum," *Proceedings of the National Academy of Sciences*, vol. 113, no. 38, pp. 10 473–10 478, 2016.

[59] D. K. Oh, T. Lee, B. Ko, T. Badloe, J. G. Ok, and J. Rho, "Nanoimprint lithography for high-throughput fabrication of metasurfaces," *Frontiers of Optoelectronics*, vol. 14, no. 2, pp. 229–251, 2021.

[60] M. L. Fajri, N. Kossowski, I. Bouanane, F. Bedu, P. Poungsripong, R. Juliano-Martins, C. Majorel, O. Margeat, J. Le Rouzo, P. Genevet, and B. Sciacca, "Designer Metasurfaces via Nanocube Assembly at the Air–Water Interface," *ACS Nano*, p. acsnano.4c06022, 2024.

[61] J. Sisler, P. Thureja, M. Y. Grajower, R. Sokhoyan, I. Huang, and H. A. Atwater, "Electrically tunable space–time metasurfaces at optical frequencies," *Nature Nanotechnology*, vol. 19, no. 10, pp. 1491–1498, 2024.

[62] E. Klopfer, H. C. Delgado, S. Dagli, M. Lawrence, and J. A. Dionne, "A thermally controlled high-Q metasurface lens," *Applied Physics Letters*, vol. 122, no. 22, p. 221701, 2023.

[63] S.-Q. Li, X. Xu, R. Maruthiyodan Veetil, V. Valuckas, R. Paniagua-Domínguez, and A. I. Kuznetsov, "Phase-only transmissive spatial light modulator based on tunable dielectric metasurface," *Science*, vol. 364, no. 6445, pp. 1087–1090, 2019.

[64] G. Zheng, H. Mühlenbernd, M. Kenney, G. Li, T. Zentgraf, and S. Zhang, "Metasurface holograms reaching 80% efficiency," *Nature Nanotechnology*, vol. 10, no. 4, pp. 308–312, 2015.

[65] G. Pan, M. Xun, X. Zhou, Y. Sun, Y. Dong, and D. Wu, "Harnessing the capabilities of VCSELs: unlocking the potential for advanced integrated photonic devices and systems," *Light: Science & Applications*, vol. 13, no. 1, p. 229, 2024.

[66] H. Li, D. B. Phillips, X. Wang, Y.-L. D. Ho, L. Chen, X. Zhou, J. Zhu, S. Yu, and X. Cai, "Orbital angular momentum vertical-cavity surface-emitting lasers," *Optica*, vol. 2, no. 6, p. 547, 2015.

[67] M. S. Seghilani, M. Myara, M. Sellahi, L. Legratiet, I. Sagnes, G. Beaudoin, P. Lalanne, and A. Garnache, "Vortex Laser based on III-V semiconductor metasurface: direct generation of coherent Laguerre-Gauss modes carrying controlled orbital angular momentum," *Scientific Reports*, vol. 6, no. 1, p. 38156, 2016.

[68] Y.-Y. Xie, P.-N. Ni, Q.-H. Wang, Q. Kan, G. Briere, P.-P. Chen, Z.-Z. Zhao, A. Delga, H.-R. Ren, H.-D. Chen, C. Xu, and P. Genevet, "Metasurface-integrated vertical cavity surface-emitting lasers for programmable directional lasing emissions," *Nature Nanotechnology*, vol. 15, no. 2, pp. 125–130, 2020.

[69] Q. Wang, P. Ni, Y. Xie, Q. Kan, P. Chen, P. Fu, J. Deng, T. Jin, H. Chen, H. W. H. Lee, C. Xu, and P. Genevet, "On-Chip Generation of Structured Light Based on Metasurface Optoelectronic Integration," *Laser & Photonics Reviews*, vol. 15, no. 3, p. 2000385, 2021.

[70] L. Bao, B. Wu, R. Y. Wu, Q. Wang, X. Pei, H. Zhang, P. P. Chen, C. Xu, Q. Kan, T. J. Cui, and Y. Xie, "On-chip multidimensional manipulations of spatial laser fields by jointly controlling amplitude and phase of metasurface," *Advanced Functional Materials*, vol. 35, no. 9, p. 2415983, 2025.

[71] X. Pei, P. Chang, L. Bao, B. Wu, Q. Wang, Z. Ma, C. Xu, Q. Kan, and Y. Xie, "Metasurface-integrated VCSEL and metalens cascade for line-shaped top-hat beam generation," *Optics Express*, vol. 34, no. 5, p. 7662, 2026.

[72] B. Wu, Q. Wang, Z. Ma, L. Bao, J. Deng, C. Xu, L. Liu, Q. Kan, and Y. Xie, "Metasurface-integrated vertical-cavity surface-emitting lasers with adaptive beam control for high-temperature stable operation," *Photonics Research*, vol. 14, no. 3, p. 676, 2026.

[73] P.-N. Ni, P. Fu, P.-P. Chen, C. Xu, Y.-Y. Xie, and P. Genevet, "Spin-decoupling of vertical cavity surface-emitting lasers with complete phase modulation using on-chip integrated Jones matrix metasurfaces," *Nature Communications*, vol. 13, no. 1, p. 7795, 2022.

[74] P. Fu, P. Ni, B. Wu, X. Pei, Q. Wang, P. Chen, C. Xu, Q. Kan, W. Chu, and Y. Xie, "Metasurface Enabled On-Chip Generation and Manipulation of Vector Beams from Vertical Cavity Surface-Emitting Lasers," *Advanced Materials*, vol. 35, no. 12, p. 2204286, 2023.

[75] X. Pei, L. Bao, Q. Wang, B. Wu, P. Fu, H. Zhou, J. Deng, P. Ni, Q. Kan, P. Chen, and Y. Xie, "On-chip integration of metasurface-based beam splitter with variable split ratio," *Laser & Photonics Reviews*, vol. 19, no. 16, p. 2500140, 2025.

[76] B. Wu, C.-L. Zheng, X.-C. Liu, Q.-H. Wang, J. Deng, Z.-T. Ma, C. Xu, P.-N. Ni, Q. Kan, and Y.-Y. Xie, "Directional perfect poincaré beams generated by spin-decoupling of VCSELs using integrated metasurfaces," *Nano Letters*, vol. 25, no. 38, pp. 14 002–14 009, 2025.

[77] Y. Ji, Y. Cui, B. Zhao, S. Li, Z. Zhang, H. Hu, J. Wang, C. Shen, and C. J. Chang-Hasnain, "4x4 back-emitting VCSEL array with integrated HCG metalens for high-speed optical interconnects," *Vertical-Cavity Surface-Emitting Lasers XXX*, C. Lei and L. A. Graham, Eds. San Francisco, United States: SPIE, 2026, p. 20.

[78] D. Wen, J. Meng, J. J. Cadusch, and K. B. Crozier, "VCSELs with On-Facet Metasurfaces for Polarization State Generation and Detection," *Advanced Optical Materials*, vol. 9, no. 9, p. 2001780, 2021.

[79] X. Jia, J. Kapraun, J. Wang, J. Qi, Y. Ji, and C. Chang-Hasnain, "Metasurface reflector enables room-temperature circularly polarized emission from VCSEL," *Optica*, vol. 10, no. 8, p. 1093, 2023.

[80] H. Kroemer, "A proposed class of hetero-junction injection lasers," *Proceedings of the IEEE*, vol. 51, no. 12, pp. 1782–1783, 1963.

[81] I. Hayashi, M. B. Panish, P. W. Foy, and S. Sumski, "Junction Lasers which Operate Continuously at Room Temperature," *Applied Physics Letters*, vol. 17, no. 3, pp. 109–111, 1970.

[82] M. Fox and R. Ispasoiu, "Quantum Wells, Superlattices, and Band-Gap Engineering," in *Springer Handbook of Electronic and Photonic Materials*, S. Kasap and P. Capper, Eds. Cham: Springer International Publishing, 2017, pp. 1–1, series Title: Springer Handbooks.

[83] C. Kittel, *Introduction to Solid State Physics*, 8th ed. Hoboken, NJ: Wiley, 2004.

[84] P. S. Zory, *Quantum Well Lasers*, ser. Quantum electronics–principles and applications. Boston: Academic Press, 1993.

[85] N. Holonyak, R. Kolbas, R. Dupuis, and P. Dapkus, "Quantum-well heterostructure lasers," *IEEE Journal of Quantum Electronics*, vol. 16, no. 2, pp. 170–186, 1980.

[86] A. Larsson and J. S. Gustavsson, "Single-Mode VCSELs," in *VCSELs*, R. Michalzik, Ed. Berlin, Heidelberg: Springer Berlin Heidelberg, 2013, vol. 166, pp. 119–144, series Title: Springer Series in Optical Sciences.

[87] E. O'Reilly and A. Adams, "Band-structure engineering in strained semiconductor lasers," *IEEE Journal of Quantum Electronics*, vol. 30, no. 2, pp. 366–379, 1994.

[88] M. Asada, A. Kameyama, and Y. Suematsu, "Gain and intervalence band absorption in quantum-well lasers," *IEEE Journal of Quantum Electronics*, vol. 20, no. 7, pp. 745–753, 1984.

[89] M. Hagerott Crawford, R. Schneider, K. Choquette, K. Lear, S. Kilcoyne, and J. Figiel, "High efficiency AlGaInP-based 660–680 nm vertical-cavitysurfaceemitting lasers," *Electronics Letters*, vol. 31, no. 3, pp. 196–198, 1995.

[90] M. Wistey, S. Bank, H. Bae, H. Yuen, E. Pickett, L. Goddard, and J. Harris, "GaInNAsSb/GaAs vertical cavity surface emitting lasers at 1534 nm," *Electronics Letters*, vol. 42, no. 5, pp. 282–283, 2006.

[91] M. E. Barnes, Z. Mihoubi, K. G. Wilcox, A. H. Quarterman, I. Farrer, D. A. Ritchie, A. Garnache, S. Hoogland, V. Apostolopoulos, and A. C. Tropper, "Gain bandwidth characterization of surface-emitting quantum well laser gain structures for femtosecond operation," *Optics Express*, vol. 18, no. 20, p. 21330, 2010.

[92] B. E. A. Saleh and M. C. Teich, *Fundamentals of Photonics*, 1st ed. Wiley, 1991.

[93] C. Mateus, M. Huang, Y. Deng, A. Neureuther, and C. Chang-Hasnain, "Ultrabroadband Mirror Using Low-Index Cladded Subwavelength Grating," *IEEE Photonics Technology Letters*, vol. 16, no. 2, pp. 518–520, 2004.

[94] M. C. Huang, Y. Zhou, and C. J. Chang-Hasnain, "A surface-emitting laser incorporating a high-index-contrast subwavelength grating," *Nature Photonics*, vol. 1, no. 2, pp. 119–122, 2007.

[95] Y. Varshni, "Temperature dependence of the energy gap in semiconductors," *Physica*, vol. 34, no. 1, pp. 149–154, 1967.

[96] A. Zielińska, A. Musiał, P. Wyborski, M. Kuniej, T. Heuser, N. Srocka, J. Grosse, J. P. Reithmaier, M. Benyoucef, S. Rodt, S. Reitzenstein, and W. Rudno-Rudziński, "Temperature dependence of refractive indices of $Al_{0.9}$ $Ga_{0.1}$ As and $In_{0.53}$ $Al_{0.1}$ $Ga_{0.37}$ As in the telecommunication spectral range," *Optics Express*, vol. 30, no. 12, p. 20225, 2022.

[97] Y.-C. Chang and L. A. Coldren, "Design and Performance of High-Speed VCSELs," in *VCSELs*, R. Michalzik, Ed. Berlin, Heidelberg: Springer Berlin Heidelberg, 2013, vol. 166, pp. 233–262, series Title: Springer Series in Optical Sciences.

[98] B. W. Hakki and T. L. Paoli, "Gain spectra in GaAs double-heterostructure injection lasers," *Journal of Applied Physics*, vol. 46, no. 3, pp. 1299–1306, 1975.

[99] Kai-Lun Chi, Jia-Liang Yen, Jhih-Min Wun, Jia-Wei Jiang, I-Cheng Lu, J. Chen, Ying-Jay Yang, and Jin-Wei Shi, "Strong wavelength detuning of 850 nm vertical-cavity surface-emitting lasers for high-speed (>40 gbit/s) and low-energy consumption operation," *IEEE Journal of Selected Topics in Quantum Electronics*, vol. 21, no. 6, pp. 470–479, 2015.

[100] K. Choquette, R. Schneider, K. Lear, and K. Geib, "Low threshold voltage vertical-cavity lasers fabricated by selective oxidation," *Electronics Letters*, vol. 30, no. 24, pp. 2043–2044, 1994.

[101] J. M. Dallesasse, N. Holonyak, A. R. Sugg, T. A. Richard, and N. El-Zein, "Hydrolyzation oxidation of AlGaAs-AlAs-GaAs quantum well heterostructures and superlattices," *Applied Physics Letters*, vol. 57, no. 26, pp. 2844–2846, 1990.

[102] B. Weigl, M. Grabherr, C. Jung, R. Jager, G. Reiner, R. Michalzik, D. Sowada, and K. Ebeling, "High-performance oxide-confined GaAs VCSELs," *IEEE Journal of Selected Topics in Quantum Electronics*, vol. 3, no. 2, pp. 409–415, 1997.

[103] E. Haglund, P. Westbergh, J. S. Gustavsson, E. P. Haglund, and A. Larsson, "High-Speed VCSELs With Strong Confinement of Optical Fields and Carriers," *Journal of Lightwave Technology*, vol. 34, no. 2, pp. 269–277, 2016.

[104] K. D. Choquette, W. W. Chow, G. R. Hadley, H. Q. Hou, and K. M. Geib, "Scalability of small-aperture selectively oxidized vertical cavity lasers," *Applied Physics Letters*, vol. 70, no. 7, pp. 823–825, 1997.

[105] D. C. Hall, H. Wu, L. Kou, Y. Luo, R. J. Epstein, O. Blum, and H. Hou, "Refractive index and hygroscopic stability of $Al_xGa_{(1-x)}As$ native oxides," *Applied Physics Letters*, vol. 75, no. 8, pp. 1110–1112, 1999.

[106] F. Sfigakis, P. Paddon, V. Pacradouni, M. Adamcyk, C. Nicoll, A. Cowan, T. Tiedje, and J. Young, "Near-infrared refractive index of thick, laterally oxidized AlGaAs cladding layers," *Journal of Lightwave Technology*, vol. 18, no. 2, pp. 199–202, 2000.

[107] K. Choquette, K. Geib, C. Ashby, R. Twesten, O. Blum, H. Hou, D. Follstaedt, B. Hammons, D. Mathes, and R. Hull, "Advances in selective wet oxidation of AlGaAs alloys," *IEEE Journal of Selected Topics in Quantum Electronics*, vol. 3, no. 3, pp. 916–926, 1997.

[108] G. R. Hadley, "Effective index model for vertical-cavity surface-emitting lasers," *Optics Letters*, vol. 20, no. 13, p. 1483, 1995.

[109] G. Hadley, K. Lear, M. Warren, K. Choquette, J. Scott, and S. Corzine, "Comprehensive numerical modeling of vertical-cavity surface-emitting lasers," *IEEE Journal of Quantum Electronics*, vol. 32, no. 4, pp. 607–616, 1996.

[110] K. Shigihara, Y. Nagai, S. Karakida, A. Takami, Y. Kokubo, H. Matsubara, and S. Kakimoto, "High-power operation of broad-area laser diodes with GaAs and AlGaAs single quantum wells for Nd:YAG laser pumping," *IEEE Journal of Quantum Electronics*, vol. 27, no. 6, pp. 1537–1543, 1991.

[111] G. Van Der Sande, M. Peeters, I. Veretennicoff, J. Danckaert, G. Verschaffelt, and S. Balle, "The Effects of Stress, Temperature, and Spin Flips on Polarization Switching in Vertical-Cavity Surface-Emitting Lasers," *IEEE Journal of Quantum Electronics*, vol. 42, no. 9, pp. 896–9, 2006.

[112] A. e. a. Quirce, "Analysis of the polarization of single-mode vertical-cavity surface-emitting lasers subject to parallel optical injection," *Journal of the Optical Society of America B*, vol. 34, no. 2, p. 447, 2017.

[113] B. Ryvkin, K. Panajotov, A. Georgievski, J. Danckaert, M. Peeters, G. Verschaffelt, H. Thienpont, and I. Veretennicoff, "Effect of photon-energy-dependent loss and gain mechanisms on polarization switching in vertical-cavity surface-emitting lasers," *Journal of the Optical Society of America B*, vol. 16, no. 11, p. 2106, 1999.

[114] J. Danckaert, M. Peeters, C. Mirasso, M. SanMiguel, G. Verschaffelt, J. Albert, B. Nagler, H. Unold, R. Michalzik, G. Giacomelli, and F. Marin, "Stochastic Polarization Switching Dynamics in Vertical-Cavity Surface-Emitting Lasers: Theory and Experiment," *IEEE Journal of Selected Topics in Quantum Electronics*, vol. 10, no. 5, pp. 911–917, 2004.

[115] B. Nagler, M. Peeters, J. Albert, G. Verschaffelt, K. Panajotov, H. Thienpont, I. Veretennicoff, J. Danckaert, S. Barbay, G. Giacomelli, and F. Marin, "Polarization-mode hopping in single-mode vertical-cavity surface-emitting lasers: Theory and experiment," *Physical Review A*, vol. 68, no. 1, p. 013813, 2003.

[116] G. Verschaffelt, J. Albert, B. Nagler, M. Peeters, J. Danckaert, S. Barbay, G. Giacomelli, and F. Marin, "Frequency response of polarization switching in vertical-cavity surface-emitting lasers," *IEEE Journal of Quantum Electronics*, vol. 39, no. 10, pp. 1177–1186, 2003.

[117] J. S. Gustavsson, Å. Haglund, J. A. Vukušić, J. Bengtsson, P. Jedrasik, and A. Larsson, "Efficient and individually controllable mechanisms for mode and polarization selection in VCSELs, based on a common, localized, sub-wavelength surface grating," *Optics Express*, vol. 13, no. 17, p. 6626, 2005.

[118] Å. Haglund, J. S. Gustavsson, J. Bengtsson, P. Jedrasik, and A. Larsson, "Design and Evaluation of Fundamental-Mode and Polarization-Stabilized VCSELs With a Subwavelength Surface Grating," *IEEE Journal of Quantum Electronics*, vol. 42, no. 3, pp. 231–240, 2006.

[119] E. Hecht, *Optics*, 5th ed. Boston Columbus Indianapolis New York San Francisco Amsterdam Cape Town Dubai London Madrid Milan Munich: Pearson, 2017.

[120] E. Strandberg, M. Juodenas, A. Grabowski, A. Haglund, and A. Larsson, "Buried Subwavelength Gratings for Polarization Pinning of Bottom-Emitting GaAs VCSELs," *IEEE Journal of Selected Topics in Quantum Electronics*, vol. 32, no. 6: Special Issue on Advances in, pp. 1 701 408–1 701 408, 2026.

[121] A. I. Kuznetsov, A. E. Miroshnichenko, M. L. Brongersma, Y. S. Kivshar, and B. Luk'yanchuk, "Optically resonant dielectric nanostructures," *Science*, vol. 354, no. 6314, p. aag2472, 2016.

[122] E. Rousseau and D. Felbacq, "Concept of a Generalized Law of Refraction: A Phenomenological Model," *ACS Photonics*, vol. 7, no. 7, pp. 1649–1654, 2020.

[123] Z. Zalevsky, R. G. Dorsch, and D. Mendlovic, "Gerchberg–Saxton algorithm applied in the fractional Fourier or the Fresnel domain," *Optics Letters*, vol. 21, no. 12, p. 842, 1996.

[124] X. Ni, A. V. Kildishev, and V. M. Shalaev, "Metasurface holograms for visible light," *Nature Communications*, vol. 4, no. 1, p. 2807, 2013.

[125] Z. Liu, D. Zhu, S. P. Rodrigues, K.-T. Lee, and W. Cai, "Generative Model for the Inverse Design of Metasurfaces," *Nano Letters*, vol. 18, no. 10, pp. 6570–6576, 2018.

[126] T. Gahlmann and P. Tassin, "Deep neural networks for the prediction of the optical properties and the free-form inverse design of metamaterials," *Physical Review B*, vol. 106, no. 8, p. 085408, 2022.

[127] S. Molesky, Z. Lin, A. Y. Piggott, W. Jin, J. Vucković, and A. W. Rodriguez, "Inverse design in nanophotonics," *Nature Photonics*, vol. 12, no. 11, pp. 659–670, 2018.

[128] P. Lalanne and P. Chavel, "Metalenses at visible wavelengths: past, present, perspectives," *Laser & Photonics Reviews*, vol. 11, no. 3, p. 1600295, 2017.

[129] A. Arbabi, Y. Horie, A. J. Ball, M. Bagheri, and A. Faraon, "Subwavelength-thick lenses with high numerical apertures and large efficiency based on high-contrast transmitarrays," *Nature Communications*, vol. 6, no. 1, p. 7069, 2015.

[130] M. Decker, I. Staude, M. Falkner, J. Dominguez, D. N. Neshev, I. Brener, T. Pertsch, and Y. S. Kivshar, "High-Efficiency Dielectric Huygens' Surfaces," *Advanced Optical Materials*, vol. 3, no. 6, pp. 813–820, 2015.

[131] W. Liu and Y. S. Kivshar, "Generalized Kerker effects in nanophotonics and meta-optics," *Optics Express*, vol. 26, no. 10, p. 13085, 2018.

[132] Q. Wang, E. T. F. Rogers, B. Gholipour, C.-M. Wang, G. Yuan, J. Teng, and N. I. Zheludev, "Optically reconfigurable metasurfaces and photonic devices based on phase change materials," *Nature Photonics*, vol. 10, no. 1, pp. 60–65, 2016.

[133] M. Rahmani, L. Xu, A. E. Miroshnichenko, A. Komar, R. Camacho-Morales, H. Chen, Y. Zárate, S. Kruk, G. Zhang, D. N. Neshev, and Y. S. Kivshar, "Reversible Thermal Tuning of All-Dielectric Metasurfaces," *Advanced Functional Materials*, vol. 27, no. 31, p. 1700580, 2017.

[134] M. Sun, X. Xu, X. W. Sun, X. Liang, V. Valuckas, Y. Zheng, R. Paniagua-Domínguez, and A. I. Kuznetsov, "Efficient visible light modulation based on electrically tunable all dielectric metasurfaces embedded in thin-layer nematic liquid crystals," *Scientific Reports*, vol. 9, no. 1, p. 8673, 2019.

[135] P. Moitra, X. Xu, R. Maruthiyodan Veetil, X. Liang, T. W. W. Mass, A. I. Kuznetsov, and R. Paniagua-Domínguez, "Electrically Tunable Reflective Metasurfaces with Continuous and Full-Phase Modulation for High-Efficiency Wavefront Control at Visible Frequencies," *ACS Nano*, vol. 17, no. 17, pp. 16 952–16 959, 2023.

[136] S. Pancharatnam, "Generalized theory of interference, and its applications: Part I. Coherent pencils," *Proceedings of the Indian Academy of Sciences - Section A*, vol. 44, no. 5, pp. 247–262, 1956.

[137] M. Berry, "The Adiabatic Phase and Pancharatnam's Phase for Polarized Light," *Journal of Modern Optics*, vol. 34, no. 11, pp. 1401–1407, 1987.

[138] A. Arbabi, Y. Horie, M. Bagheri, and A. Faraon, "Dielectric metasurfaces for complete control of phase and polarization with subwavelength spatial resolution and high transmission," *Nature Nanotechnology*, vol. 10, no. 11, pp. 937–943, 2015.

[139] J. Balthasar Mueller, N. A. Rubin, R. C. Devlin, B. Groever, and F. Capasso, "Metasurface Polarization Optics: Independent Phase Control of Arbitrary Orthogonal States of Polarization," *Physical Review Letters*, vol. 118, no. 11, p. 113901, 2017.

[140] H.-X. Xu, L. Han, Y. Li, Y. Sun, J. Zhao, S. Zhang, and C.-W. Qiu, "Completely Spin-Decoupled Dual-Phase Hybrid Metasurfaces for Arbitrary Wavefront Control," *ACS Photonics*, vol. 6, no. 1, pp. 211–220, 2019.

[141] Y. Guo, S. Zhang, M. Pu, Q. He, J. Jin, M. Xu, Y. Zhang, P. Gao, and X. Luo, "Spin-decoupled metasurface for simultaneous detection of spin and orbital angular momenta via momentum transformation," *Light: Science & Applications*, vol. 10, no. 1, p. 63, 2021.

[142] Y. Qiu, S. Tang, T. Cai, H. Xu, and F. Ding, "Fundamentals and applications of spin-decoupled Pancharatnam—Berry metasurfaces," *Frontiers of Optoelectronics*, vol. 14, no. 2, pp. 134–147, 2021.

[143] Y. Ra'di, D. L. Sounas, and A. Alù, "Metagratings: Beyond the Limits of Graded Metasurfaces for Wave Front Control," *Physical Review Letters*, vol. 119, no. 6, p. 067404, 2017.

[144] R. Paniagua-Domínguez, Y. F. Yu, E. Khaidarov, S. Choi, V. Leong, R. M. Bakker, X. Liang, Y. H. Fu, V. Valuckas, L. A. Krivitsky, and A. I. Kuznetsov, "A Metalens with a Near-Unity Numerical Aperture," *Nano Letters*, vol. 18, no. 3, pp. 2124–2132, 2018.

[145] M. Juodėnas, E. Strandberg, A. Grabowski, J. Gustavsson, H. Šípová Jungová, A. Larsson, and M. Käll, "High-angle deflection of metagrating-integrated laser emission for high-contrast microscopy," *Light: Science & Applications*, vol. 12, no. 1, p. 251, 2023.

[146] M. G. Moharam and T. K. Gaylord, "Rigorous coupled-wave analysis of grating diffraction— E-mode polarization and losses," *Journal of the Optical Society of America*, vol. 73, no. 4, p. 451, 1983.

[147] V. Liu and S. Fan, "S4 : A free electromagnetic solver for layered periodic structures," *Computer Physics Communications*, vol. 183, no. 10, pp. 2233–2244, 2012.

[148] J. Martínez-Llinàs, C. Henry, D. Andrén, R. Verre, M. Käll, and P. Tassin, "A Gaussian reflective metasurface for advanced wavefront manipulation," *Optics Express*, vol. 27, no. 15, p. 21069, 2019.

[149] M. A. Afromowitz, "Refractive index of $Ga_{1-x}Al_xAs$," *Solid State Communications*, vol. 15, no. 1, pp. 59–63, 1974.

[150] T. Rylander, P. Ingelström, and A. Bondeson, *Computational Electromagnetics*, ser. Texts in Applied Mathematics, S. S. Antman, P. Holmes, and K. Sreenivasan, Eds. New York, NY: Springer New York, 2013.

[151] A. Taflove, A. Oskooi, and S. G. Johnson, Eds., *Advances in FDTD computational electrodynamics: photonics and nanotechnology*, ser.

Artech House antennas and propagation series. Boston: Artech House, 2013.

[152] B. Schaefer, E. Collett, R. Smyth, D. Barrett, and B. Fraher, "Measuring the stokes polarization parameters," *American Journal of Physics*, vol. 75, no. 2, pp. 163–168, 2007.

[153] H. G. Berry, G. Gabrielse, and A. E. Livingston, "Measurement of the Stokes parameters of light," *Applied Optics*, vol. 16, no. 12, p. 3200, 1977.

[154] K. Vahlin, "Large-angle deflection lens using supercell metasurfaces," 2024.

[155] R. Yuste, "Fluorescence microscopy today," *Nature Methods*, vol. 2, no. 12, pp. 902–904, 2005.

[156] Y. M. Sigal, R. Zhou, and X. Zhuang, "Visualizing and discovering cellular structures with super-resolution microscopy," *Science*, vol. 361, no. 6405, pp. 880–887, 2018.

[157] L. A. Masullo, A. Bodén, F. Pennacchietti, G. Coceano, M. Ratz, and I. Testa, "Enhanced photon collection enables four dimensional fluorescence nanoscopy of living systems," *Nature Communications*, vol. 9, no. 1, p. 3281, 2018.

[158] L. Schermelleh, A. Ferrand, T. Huser, C. Eggeling, M. Sauer, O. Biehlmaier, and G. P. C. Drummen, "Super-resolution microscopy demystified," *Nature Cell Biology*, vol. 21, no. 1, pp. 72–84, 2019.

[159] D. Huang, E. A. Swanson, C. P. Lin, J. S. Schuman, W. G. Stinson, W. Chang, M. R. Hee, T. Flotte, K. Gregory, C. A. Puliafito, and J. G. Fujimoto, "Optical Coherence Tomography," *Science*, vol. 254, no. 5035, pp. 1178–1181, 1991.

[160] A. Ashkin, "Optical trapping and manipulation of neutral particles using lasers," *Proceedings of the National Academy of Sciences*, vol. 94, no. 10, pp. 4853–4860, 1997.

[161] P. Paramasivam, C. Franke, M. Stöter, A. Höijer, S. Bartesaghi, A. Sabirsh, L. Lindfors, M. Y. Arteta, A. Dahlén, A. Bak, S. Andersson, Y. Kalaidzidis, M. Bickle, and M. Zerial, "Endosomal es-

cape of delivered mRNA from endosomal recycling tubules visualized at the nanoscale," *Journal of Cell Biology*, vol. 221, no. 2, p. e202110137, 2022.

[162] P. N. Prasad, *Introduction to biophotonics*. Hoboken, NJ: Wiley-Interscience, 2003.

[163] F. Vollmer and S. Arnold, "Whispering-gallery-mode biosensing: label-free detection down to single molecules," *Nature Methods*, vol. 5, no. 7, pp. 591–596, 2008.

[164] K. Padmaraju and K. Bergman, "Resolving the thermal challenges for silicon microring resonator devices," *Nanophotonics*, vol. 3, no. 4-5, pp. 269–281, 2014.

[165] T. Laksanasopin, T. W. Guo, S. Nayak, A. A. Sridhara, S. Xie, O. O. Olowookere, P. Cadinu, F. Meng, N. H. Chee, J. Kim, C. D. Chin, E. Munyazesa, P. Mugwaneza, A. J. Rai, V. Mugisha, A. R. Castro, D. Steinmiller, V. Linder, J. E. Justman, S. Nsanzimana, and S. K. Sia, "A smartphone dongle for diagnosis of infectious diseases at the point of care," *Science Translational Medicine*, vol. 7, no. 273, 2015.

[166] J. Kim, A. S. Campbell, B. E.-F. De Ávila, and J. Wang, "Wearable biosensors for healthcare monitoring," *Nature Biotechnology*, vol. 37, no. 4, pp. 389–406, 2019.

[167] T. Thorsen, S. J. Maerkl, and S. R. Quake, "Microfluidic Large-Scale Integration," *Science*, vol. 298, no. 5593, pp. 580–584, 2002.

[168] G. M. Whitesides, "The origins and the future of microfluidics," *Nature*, vol. 442, no. 7101, pp. 368–373, 2006.

[169] J. Kim, D. Taylor, N. Agrawal, H. Wang, H. Kim, A. Han, K. Rege, and A. Jayaraman, "A programmable microfluidic cell array for combinatorial drug screening," *Lab on a Chip*, vol. 12, no. 10, p. 1813, 2012.

[170] J. Homola, "Surface Plasmon Resonance Sensors for Detection of Chemical and Biological Species," *Chemical Reviews*, vol. 108, no. 2, pp. 462–493, 2008.

[171] J. N. Anker, W. P. Hall, O. Lyandres, N. C. Shah, J. Zhao, and R. P. Van Duyne, "Biosensing with plasmonic nanosensors," *Nature Materials*, vol. 7, no. 6, pp. 442–453, 2008.

[172] B. Liedberg, C. Nylander, and I. Lunström, "Surface plasmon resonance for gas detection and biosensing," *Sensors and Actuators*, vol. 4, pp. 299–304, 1983.

[173] K. Matsubara, S. Kawata, and S. Minami, "Multilayer system for a high-precision surface plasmon resonance sensor," *Optics Letters*, vol. 15, no. 1, p. 75, 1990.

[174] M. Piliarik and J. Homola, "Surface plasmon resonance (SPR) sensors: approaching their limits?" *Optics Express*, vol. 17, no. 19, p. 16505, 2009.

[175] A. Ashkin, J. M. Dziedzic, J. E. Bjorkholm, and S. Chu, "Observation of a single-beam gradient force optical trap for dielectric particles," *Optics Letters*, vol. 11, no. 5, p. 288, 1986.

[176] K. C. Neuman and A. Nagy, "Single-molecule force spectroscopy: optical tweezers, magnetic tweezers and atomic force microscopy," *Nature Methods*, vol. 5, no. 6, pp. 491–505, 2008.

[177] R. A. Flynn, A. L. Birkbeck, M. Gross, M. Ozkan, B. Shao, M. M. Wang, and S. C. Esener, "Parallel transport of biological cells using individually addressable VCSEL arrays as optical tweezers," *Sensors and Actuators B: Chemical*, vol. 87, no. 2, pp. 239–243, 2002.

[178] A. L. Birkbeck, R. A. Flynn, M. Ozkan, D. Song, M. Gross, and S. C. Esener, "VCSEL Arrays as Micromanipulators in Chip-Based Biosystems," *Biomedical Microdevices*, vol. 5, no. 1, pp. 47–54, 2003.

[179] B. Shao, S. Zlatanovic, M. Ozkan, A. L. Birkbeck, and S. C. Esener, "Manipulation of microspheres and biological cells with multiple agile VCSEL traps," *Sensors and Actuators B: Chemical*, vol. 113, no. 2, pp. 866–874, 2006.

[180] A. Kroner, C. Schneck, F. Rinaldi, R. Rösch, and R. Michalzik, "Application of vertical-cavity laser-based optical tweezers for particle manipulation in microfluidic channels," D. L. Andrews, J.-

M. Nunzi, and A. Ostendorf, Eds., Strasbourg, France, 2008, p. 69881R.

[181] G. Pesce, P. H. Jones, O. M. Maragò, and G. Volpe, "Optical tweezers: theory and practice," *The European Physical Journal Plus*, vol. 135, no. 12, p. 949, 2020.